Research Square

Preprints are preliminary reports that have not undergone peer review.
They should not be considered conclusive, used to inform clinical practice,
or referenced by the media as validated information.

Micron-scale Quantum Dot Light-Emitting Diodes with EQE Exceeding 42%

Hailong Hu

huhl@fzu.edu.cn

Fuzhou University https://orcid.org/0000-0001-5299-2812

Hao Liu

Fuzhou University

Kuibao Yu

Institute of Optoelectronic Technology, Fuzhou University

Tian Liu

Fuzhou University

Jiahao Wang

Fuzhou University

Kai Xie

Fuzhou University

Haolin Luo

Fuzhou University

Zhihan Lin

Fuzhou University

Jingnan Su

Fuzhou University

Guihua Lin

Fuzhou University

Peijun Wang

Fuzhou University

Weiguo Chen

Fuzhou University

Kaiyu Yang

Institute of Optoelectronic Technology, Fuzhou University https://orcid.org/0000-0001-8910-8197

Fushan Li

Institute of Optoelectronic Technology, Fuzhou University https://orcid.org/0000-0002-2436-9473

Article

Keywords: Tandem QLEDs, Charge generation layer, Energy level modulation, Defect passivation, Interfacial engineering

Posted Date: July 24th, 2026

DOI: https://doi.org/10.21203/rs.3.rs-10257362/v1

License: This work is licensed under a Creative Commons Attribution 4.0 International License. Read Full License

Additional Declarations: There is **NO** Competing Interest.

Micron-scale Quantum Dot Light-Emitting Diodes with EQE Exceeding 42%

Hao Liu[1,†], Kuibao Yu[1,†], Tian Liu[1], Jiahao Wang[1], Kai Xie[1], Haolin Luo[1], Zhihan Lin[1], Jingnan Su[1], Guihua Lin[1], Peijun Wang[1], Weiguo Chen[1], Kaiyu Yang[1], Fushan Li[1,2,*], Hailong Hu[1,2,*]

[1]Institute of Optoelectronic Technology, Fuzhou University, Fuzhou 350116, P. R. China

[2]Fujian Science and Technology Innovation Laboratory for Optoelectronic Information of China, Fuzhou 350108, P. R. China

E-mail addresses: huhl@fzu.edu.cn (H. Hu); fsli@fzu.edu.cn (F. Li)

[†]These authors contributed equally: Hao Liu and Kuibao Yu

Abstract

Ultrahigh-resolution quantum dot light-emitting diodes (QLEDs) are promising building blocks for next-generation near-eye micro-displays, yet pixel-edge electric field distortion induces an intrinsic efficiency-resolution trade-off that severely hinders their practical deployment. Tandem architectures enable prominent electroluminescence enhancement, but their implementation in high-resolution patterned QLEDs remains largely unexplored, limited by the inferior charge-generation capability and high operating voltage of conventional charge generation layers (CGLs). Herein, we demonstrate the first dual-function molecularly engineered CGL for high-resolution tandem QLEDs, realizing synergistic defect passivation and electronic band

modulation of ZnO using fluorinated 4,4'-(hexafluoroisopropylidene)diphenol (BPAF). BPAF strongly coordinates with defective sites to passivate oxygen-vacancy-derived deep-level traps, while triggering spontaneous downward band bending to optimize interfacial energy alignment, thereby suppressing non-radiative recombination and lowering the interfacial charge-generation barrier. Benefiting from this dual-functional modulation, the all-solution-processed patterned QLEDs deliver a record-high external quantum efficiency of 42.82% at an ultrahigh pixel density of 10,160 PPI, fundamentally breaking the long-standing efficiency-resolution trade-off. Importantly, the high-resolution QLEDs achieve an ultra-low turn-on voltage of 2.0 V and a state-of-the-art power efficiency of 62.7 lm W^{-1}. This work opens a universal pathway toward the design of high-performance, ultrahigh-resolution QLEDs for low-power wearable near-eye display applications.

Keywords: *Tandem QLEDs; Charge generation layer; Energy level modulation; Defect passivation; Interfacial engineering*

Introduction

With cutting-edge display technologies such as augmented reality (AR), virtual reality (VR) and micro-displays continuously propelling the demands for ultra-high pixel density and precise color rendition, the core challenge of high-resolution display development has transitioned from technical feasibility verification to the scalable realization of high-efficiency light-emitting devices. Quantum dot (QD) light-emitting

diodes (QLEDs) have emerged as a compelling platform for next-generation ultra-high-resolution displays[1–4]. Unlike conventional display devices including organic light-emitting diodes (OLEDs) and Micro-LEDs, the emissive units (EMUs) of QLEDs can be miniaturized down to the single-quantum-dot scale, affording a unique and viable avenue to circumvent the pixel-size limitations of traditional display technologies[5–8]. Nevertheless, as pixels undergo continuous downsizing with lateral dimensions comparable to device thickness, patterned QLEDs confront an intrinsic resolution-efficiency trade-off that severely restricts the performance of high-resolution device[9–11]. Drastic pixel miniaturization significantly amplifies pixel boundary effects and electric field non-uniformity, which degrades the homogeneity of intra-pixel charge injection and carrier transport. Additionally, continuous pixel shrinking induces a sharp elevation in interfacial defect density, which aggravates trap-mediated non-radiative recombination of photogenerated charge carriers. Consequently, the optoelectronic efficiency of patterned QLED pixels experiences severe attenuation under ultra-high pixel per inch (PPI) operating conditions, yielding device performance far below the theoretical efficiency limit of planar non-patterned QLEDs[12–15].

To alleviate the prevalent efficiency degradation that plagues high-resolution patterned QLEDs, a series of optimization strategies have been explored, including patterning process refinement, precise modulation of carrier transport behaviors, and rational device architecture engineering. Ligand-nondestructive direct photolithography and high-precision transfer printing technologies can effectively mitigate processing-induced morphological and optoelectronic degradation of QD films,

enabling the fabrication of high-efficiency ultrahigh-resolution QLEDs[16–18]. The construction of self-assembled ordered QD emissive layers with optimized carrier injection and transport can substantially improve carrier utilization efficiency and promote radiative recombination[4,19,20]. Furthermore, the integration of a charge barrier layer (CBL) effectively inhibits leakage current and emission crosstalk in non-emissive regions, alleviating the efficiency loss triggered by direct interfacial contact between the hole transport layer (HTL) and the electron transport layer (ETL)[21,22]. In addition, the exploitation of localized surface plasmon resonance (LSPR) enables rational modulation of optical coupling between QDs and metallic nanostructures, offering an effective approach to elevate the external quantum efficiency (EQE) of high-resolution QLEDs[23]. Despite these substantial advances in narrowing the performance gap between patterned QLEDs and planar non-patterned counterparts, several intractable challenges remain unsolved. Existing optimization schemes fail to completely eliminate periodic electric field inhomogeneity and severe pixel-edge field distortion in miniaturized pixel units. In particular, high-resolution patterned QLEDs exhibit prominent efficiency roll-off under high-brightness operating conditions, which greatly deviates from their maximum EQE performance[6,12,24,25]. As the pixel dimension continues to scale down, pixel-edge electric field distortion and localized carrier accumulation become further aggravated, rendering current technical strategies incapable of breaking the performance bottlenecks of miniaturized QLED arrays.

Tandem device architectures, which vertically stack multiple optoelectronic sub-cells and adopt interconnecting layers (ICLs) to realize synchronous electrical coupling

and optical matching between adjacent functional units, offer a viable route to circumvent the inherent performance constraints of single-junction devices. This versatile architectural strategy has been extensively implemented in high-performance solar cells and OLEDs, yet its potential for boosting high-resolution patterned QLED performance remains largely underexplored[26]. In tandem light-emitting devices, the functional ICL is universally termed charge generation layer (CGL), which is conventionally realized through bilayer heterostacking of n-type and p-type semiconductor functional films to undertake interfacial charge generation and spatial charge separation. In solution-processed QLEDs, zinc oxide (ZnO) nanoparticles and PEDOT:PSS serve as the most prevalent electron transport layer (ETL) and hole transport layer (HTL), respectively, making the ZnO/PEDOT:PSS heterobilayer a highly promising CGL candidate for high-performance tandem QLEDs[27]. Nevertheless, the pristine ZnO/PEDOT:PSS CGL suffers from a relatively large energy gap between the conduction band minimum (CBM) of ZnO and the highest occupied molecular orbital (HOMO) of PEDOT:PSS. Such an unfavorable energy band alignment severely restricts interfacial charge generation and separation efficiency within the CGL. Specifically, the oversized energy barrier requires a stronger external driving electric field to trigger effective charge generation, which inevitably elevates the device turn-on voltage, deteriorates power efficiency (PE), and increases overall device power consumption. Structural engineering of periodic heterojunction-like patterns on the CGL interface has been proposed to optimize interfacial charge generation efficiency and optical coupling behavior, thus improving the overall optoelectronic performance

of tandem QLED devices[28,29]. However, such patterned modification strategies suffer from intricate fabrication procedures and poor interfacial controllability, severely limiting their practical implementation and large-scale application in high-resolution display devices. Accordingly, the rational design and construction of advanced CGL systems with efficient charge generation, suppressed interfacial energy loss, and excellent micropixel compatibility are highly imperative for the development of high-efficiency, high-resolution tandem QLED displays.

Herein, we propose a molecular modification strategy utilizing 4,4'-(hexafluoroisopropylidene)diphenol (BPAF) to construct a high-performance ZnO:BPAF/PEDOT:PSS charge generation layer (CGL) for tandem QLEDs. The BPAF dopant enables synergistic optimization involving interfacial defect passivation, energy-level alignment modulation, and built-in electric field reinforcement, collectively promoting interfacial charge generation and carrier transport kinetics within the CGL. Benefiting from the optimized CGL, the fabricated micron-scale patterned tandem QLEDs deliver a record-high external quantum efficiency (EQE) of 42.82%, while retaining superior efficiency stability at high luminance. Notably, the optimized tandem devices achieve an ultra-low turn-on voltage of 2.0 V and a state-of-the-art power efficiency of 62.7 lm W^{-1}, offering great potential for low-power-consumption display scenarios. This work establishes a facile and universal material modification and device engineering paradigm to break the inherent efficiency bottleneck of high-resolution patterned QLEDs, paving the way for the practical

deployment of tandem QLED technology in next-generation AR/VR micro-display systems.

Results and Discussion

To uncover the intrinsic mechanism by which pixel edge effects restrict the optoelectronic performance of high-resolution QLEDs, we systematically investigated the microstructural morphology and internal electric field distribution of planar non-patterned QLEDs and discrete pixelated QLED arrays via comparative analysis. As shown in Figure 1a, all functional layers of non-patterned QLEDs form a continuous fully-stacked thin-film architecture, enabling spatially homogeneous electric field distribution across the entire emissive region. Accordingly, balanced charge carrier injection and stable radiative exciton recombination can be uniformly realized over the complete light-emitting area. In contrast, pixelated QLEDs are composed of spatially discrete luminescent pixel arrays. Affected by the interfacial modulation originating from the peripheral CBL at pixel boundaries, severe electric field distortion occurs at pixel edges, accompanied by localized charge accumulation and pronounced electric field intensification near pixel peripheries (Figure 1b)[6,30]. Finite element electric field simulation results (Figure 1c, 1d) further verify that such edge-triggered electric field distortion becomes drastically aggravated with pixel dimension scaling down in ultra-high-resolution patterned QLEDs.

These spatially localized electrical inhomogeneities induce two primary detrimental impacts on device optoelectronic performance. On one hand, the intrinsic carrier

injection and transport behaviors within the QD emissive layer are severely unbalanced. On the other hand, pixel-level turn-on voltage discrepancies trigger asynchronous electroluminescence switching responses across the entire pixel array. As evidenced by current density-voltage-luminance (J-V-L) characteristics (Figure 1e) and external quantum efficiency-voltage (EQE-V) curves (Figure 1f), high-resolution pixelated QLEDs exhibit substantial efficiency degradation and exacerbated efficiency roll-off relative to planar spin-coated non-patterned counterparts. Collectively, these experimental and simulated results confirm that patterning-induced edge electric field distortion acts as an inherent performance bottleneck, fundamentally hindering the performance advancement and commercial deployment of high-resolution pixelated QLED displays[24,31].

Tandem QLED architectures, which vertically integrate multiple EMUs via intermediate charge generation layers (CGLs), have emerged as a compelling configuration to boost the external quantum efficiency of light-emitting devices. Nevertheless, intrinsic energy-level mismatch and abundant interfacial defects within conventional CGLs inevitably induce severe charge trapping, aggravated non-radiative recombination, and retarded carrier transport dynamics. These detrimental issues substantially weaken the charge generation capability of CGLs and become the major obstacle limiting further performance optimization of state-of-the-art tandem QLEDs.

To address the aforementioned CGL-related bottlenecks, this work proposes a facile interfacial engineering strategy via BPAF molecular doping of ZnO, targeted at ameliorating interfacial energy-level misalignment and eliminating intrinsic defect

states within solution-processed CGLs. The molecular configuration of BPAF is presented in Figure S1. Tandem QLEDs incorporating BPAF-modified CGLs were fabricated to validate the effectiveness of this molecular modulation strategy (Figure 2a), while the corresponding energy-level alignment and carrier transport pathways are schematically illustrated in Figure S2. Cross-sectional transmission electron microscopy (TEM) characterization (Figure 2b) confirms the well-defined multilayer stacked architecture with intact, smooth interfacial boundaries. This result demonstrates that the introduction of BPAF molecules imposes no detrimental impact on the structural integrity of solution-processed tandem multilayer devices. The precise thickness of each functional layer is summarized in Figure S3. The underlying defect passivation mechanism of BPAF toward ZnO nanoparticles is illustrated in Figure 2c. Specifically, the phenolic hydroxyl (-OH) and fluorine (-F) functional groups of BPAF enable strong coordination interactions with unsaturated Zn atoms anchored at oxygen vacancy sites on ZnO surfaces. Such robust chemical bonding effectively eliminates deep-level trap states originating from oxygen vacancies. This molecular passivation strategy successfully suppresses trap-assisted non-radiative recombination within the ZnO electron transport layer and optimizes surface band bending, substantially boosting the charge generation efficiency of CGLs[32,33].

The successful incorporation of BPAF into ZnO is verified by Fourier-transform infrared (FTIR) spectroscopy (Figure 2d), where characteristic absorption peaks assigned to C=C (1600 cm^{-1}), C-H (2850-2960 cm^{-1}), and C-F (1100-1200 cm^{-1}) bonds are clearly observed. Furthermore, X-ray diffraction (XRD) patterns (Figure 2e)

demonstrate that this surface molecular modification barely disturbs the intrinsic long-range crystalline lattice of ZnO. This evidence confirms that BPAF only modulates the local interfacial chemical environment rather than altering the bulk crystal structure of ZnO. In terms of surface micromorphology, atomic force microscopy (AFM) measurements (Figures 2f-i) reveal a distinct reduction in root-mean-square roughness (R_q). The R_q value decreases from 1.99 nm for pristine ZnO films to 1.43 nm for BPAF-modified ZnO films. Such favorable surface smoothing effect can be well maintained after the subsequent deposition of PEDOT:PSS. Specifically, the BPAF-modified ZnO/PEDOT:PSS heterojunction delivers a lower R_q of 1.00 nm, compared with 1.12 nm for the pristine counterpart. Corresponding three-dimensional AFM height topographies are supplemented in Figure S4 for intuitive comparison. Corresponding three-dimensional AFM height topographies are supplemented in Figure S4 for intuitive visual comparison. Collectively, these morphological and spectroscopic results demonstrate that BPAF modification not only optimizes ZnO surface flatness, but also improves the film-forming quality of the upper PEDOT:PSS layer, enabling compact interfacial contact and effectively suppressing leakage current and interfacial carrier-transport losses.

To further elucidate the electronic structure modulation and inherent defect passivation effect of BPAF on ZnO films, systematic spectroscopic and energy-level characterizations were performed. High-resolution X-ray photoelectron spectroscopy (XPS) O 1s spectra (Figure 3a, 3b) were deconvoluted into three characteristic peaks assigned to lattice oxygen (O_L), oxygen vacancies (O_V), and surface-adsorbed organic

oxygen (O_{org}). Quantitative peak-fitting results demonstrate that the relative proportion of oxygen vacancy defects decreases significantly from 46.88% to 31.98% after BPAF modification, providing solid evidence for the effective passivation of oxygen vacancy-related deep-level traps and the reduction of harmful interfacial defect states. High-resolution XPS Zn 2p spectra (Figure S5) exhibit negligible peak shifts for both Zn $2p_{3/2}$ and Zn $2p_{1/2}$ signals, confirming that the oxidation state of Zn^{2+} and intrinsic ZnO crystal lattice remain intact after molecular doping. Raman spectra (Figure 3c) reveal pronounced attenuation of the E_2(high) and $A_1(L_O)$ phonon modes, accompanied by narrowed longitudinal optical (L_O) phonon peak. These results confirm the suppression of defect-mediated electron–phonon coupling and the resultant non-radiative recombination loss[34–36]. Ultraviolet photoelectron spectroscopy (UPS) and ultraviolet–visible (UV-Vis) absorption measurements (Figure 3d, 3e) reveal that BPAF modification induces downward band bending of ZnO. The conduction-band minimum (E_C) shifts downward from -3.47 to -3.53 eV, and the valence-band maximum (E_V) moves from -7.05 to -7.15 eV. Meanwhile, the corresponding optical bandgap (E_g) slightly widens from 3.58 to 3.62 eV. Such optimized interfacial energy alignment indicates that BPAF engineering precisely modulates the interfacial energy landscape of ZnO, enabling efficient charge carrier injection without altering the intrinsic optical bandgap characteristics of ZnO.

The summarized energy-level diagram (Figure 3f) intuitively presents the downward shift of ZnO energy levels after BPAF decoration, which favors efficient interfacial charge separation within CGLs. Kelvin probe force microscopy (KPFM) measurements

(Figure 3g) reveal that the contact potential difference (CPD) decreases from 732.1 mV to 655.5 mV after BPAF modification, which is highly consistent with the downward band bending validated by UPS analyses. Moreover, planar KPFM potential mappings (Figure S6) further confirm improved surface potential homogeneity on the modified ZnO film. Time-resolved photoluminescence (TRPL) decay curves (Figure 3h) of QD/ZnO and QD/ZnO:BPAF bilayer films exhibit nearly identical average photoluminescence lifetimes (≈9.3 ns). This result indicates that BPAF doping barely affects the intrinsic exciton radiative decay kinetics of quantum dots. Nevertheless, the steady-state photoluminescence quantum yield (PLQY) (Figure 3i) increases sharply from 38.7% to 54.0% after BPAF treatment, verifying the effective suppression of ZnO-induced interfacial exciton quenching. Such prominent PLQY improvement originates from the efficient interfacial defect passivation enabled by BPAF molecules. The eliminated deep-level trap states block non-radiative recombination channels, preserving intrinsic radiative exciton recombination within the QD emissive layer.

To explore the electrical modulation effect of BPAF on CGL performance, standalone CGL devices were fabricated for systematic electrical characterization. The device configuration of the standalone CGL unit is displayed in the inset of Figure 4a. Under identical applied bias, the BPAF-modified CGL device exhibits a much higher current density than the pristine counterpart, confirming the substantially enhanced charge generation efficiency after molecular modification. Bipolar current-voltage (I-V) tests (Figure 4b) reveal nearly symmetric current responses of the modified device under forward and reverse biases, indicating balanced bidirectional carrier transport and

efficient in-situ interfacial charge generation. The optimized bipolar electrical characteristics further verify the lowered interfacial energy barrier and promoted charge regeneration capability of BPAF-modified CGL[37–39]. Electrochemical impedance spectroscopy (EIS) was employed to analyze the interfacial charge transfer kinetics of different CGLs, with corresponding Nyquist plots presented in Figure 4c. The BPAF-modified device exhibits a dramatically shrunk high-frequency semicircle compared with the pristine device, representing a remarkable reduction in interfacial charge transfer resistance. The decreased resistance stems from effective interfacial defect passivation and optimized energy-level alignment induced by BPAF, which accelerates interfacial carrier migration and alleviates trap-induced charge accumulation. Such accelerated interfacial charge transfer kinetics enable more efficient in-situ carrier regeneration inside CGLs, ultimately improving the charge injection capacity and electroluminescence performance of tandem QLEDs[40–43]. The fitted impedance parameters, including the high-frequency series resistance (R_s) and low-frequency recombination resistance (R), are summarized in Table 1.

Table 1. Extracted R_s and R values of pristine and BPAF-modified CGL devices.

CGL architecture	Rs	R
ZnO/PEDOT	105.6	268.7
ZnO:BPAF/PEDOT	198.6	58.72

Complementary capacitance-voltage (C-V) and normalized C/C_0-V characterizations (Figure 4d, 4e) reveal that BPAF modification increases the absolute device capacitance

while suppressing voltage-induced capacitance elevation. These results demonstrate that BPAF reinforces interfacial charge response via dipole-triggered interfacial polarization, and simultaneously mitigates excess interfacial charge accumulation through intrinsic defect passivation and homogenized charge distribution at the ZnO/QD heterointerface. Mott-Schottky analysis (Figure 4f) further verifies that the BPAF-induced interfacial dipole effect effectively elevates the built-in potential (V_{bi}) from 2.80 V to 3.01 V, corresponding to a maximum enhancement of 7.5%. Such increased V_{bi} unambiguously confirms that BPAF molecules regulate interfacial energy-level alignment via spontaneous interfacial dipole formation[44]. The strengthened built-in electric field further accelerates exciton dissociation and directional carrier migration, boosting the intrinsic charge generation efficiency of CGLs[45]. Meanwhile, the average photoluminescence (PL) lifetime decreases from 9.617 ns to 6.847 ns after BPAF functionalization, indicating accelerated interfacial charge transfer kinetics across the ZnO/QD heterojunction (Figure 4g). Such PL quenching and shortened fluorescence lifetime are commonly observed at QD/ZnO heterogeneous interfaces. Herein, the reduced decay lifetime originates from efficient interfacial charge extraction rather than aggravated non-radiative recombination. This conclusion is highly consistent with the reduced charge transfer resistance derived from the aforementioned EIS results, further validating that BPAF modification facilitates efficient charge separation and directional carrier transport within optimized CGLs[46–48]. The comprehensive charge generation and carrier transport mechanism of the BPAF-modified CGL is schematically illustrated in Figure 4h. In brief, BPAF molecular

engineering simultaneously passivates intrinsic ZnO defect states, modulates interfacial band bending, enhances the built-in electric field, and reduces interfacial charge injection barriers. Benefiting from these synergistic effects, efficient charge generation, spatial separation, and directional carrier transport are realized within the modified CGL. Detailed charge separation behaviors under varied applied biases are supplemented in Figure S7.

To further validate the device optimization efficacy of BPAF-based CGL engineering, the electroluminescence (EL) performance of pristine and modified tandem QLEDs was systematically investigated. As depicted in Figure 5a, the BPAF-optimized device achieves stable red EL emission with a narrow full-width at half-maximum (FWHM) and negligible spectral shift under varying driving voltages. Meanwhile, the EL spectrum displays a slight blue shift and reduced FWHM relative to the steady-state PL spectrum, verifying that BPAF interfacial modification nearly fully preserves the intrinsic optical merits of QD emitters. Current density-voltage-luminance (J-V-L) characteristics (Figure 5b) show that the modified device exhibits higher current density and luminance across the entire operating voltage range relative to the pristine counterpart, confirming optimized carrier injection dynamics and enhanced radiative recombination efficiency. Enabled by the prominently improved charge generation efficiency and well-balanced bidirectional carrier transport via BPAF modulation, the optimized tandem QLED achieves a remarkable EQE improvement. The maximum EQE is significantly elevated from 39.3% (pristine device) to 49.8% (BPAF-modified device) (Figure 5c). Impressively, this ultra-high EQE of 49.8%

represents the state-of-the-art performance among all-solution-processed QLEDs reported to date, establishing a new performance benchmark for solution-based tandem QLED architectures (Table S1[28,29,49–51]). Consistent with the EQE enhancement, the current efficiency is boosted from 47.6 to 64.7 cd A^{-1}, while the power efficiency is improved from 24.0 to 33.2 lm W^{-1} (Figure 5d, 5e).

To unravel the intrinsic carrier transport mechanism underlying such performance promotion, EIS measurements were performed to probe interfacial electrochemical kinetics (Figure 5f). Compared with the control device, the BPAF-modified device exhibits a markedly compressed Nyquist semicircle, indicative of reduced interfacial charge-transfer resistance[42,43]. The corresponding equivalent circuit model and detailed fitting parameters are provided in Figure S8 and Table S2, respectively. These results verify that BPAF interfacial engineering effectively alleviates interfacial charge accumulation and facilitates efficient carrier transport within tandem device architectures. To further explore the dynamic EL response characteristics, transient EL measurements were conducted under pulsed driving conditions (Figures 5g-i). Under a pulsed bias of 10 V, both pristine and optimized devices exhibit stable switching performance. Notably, the BPAF-modified device achieves faster EL rise and decay kinetics. The magnified rising-edge profile (Figure 5h) demonstrates more efficient carrier injection and accelerated interfacial charge establishment. Meanwhile, the faster decay process (Figure 5i) further confirms suppressed interfacial charge trapping and minimized trap-assisted non-radiative recombination losses in the optimized device[16–18]. Collectively, steady-state optoelectronic characterizations and transient dynamic

tests consistently validate that BPAF-mediated CGL optimization effectively balances charge generation and carrier transport, eliminates interfacial trap-induced losses, and ultimately enables prominent performance enhancement of solution-processed tandem QLEDs.

To evaluate the practical applicability of the proposed interfacial engineering strategy for high-resolution micro-display integration, patterned QLED pixel arrays with diverse geometric dimensions were fabricated via standard photolithography. AFM and scanning electron microscopy (SEM) morphological characterizations (Figures 6a-i, Figure S9 and S10) verify that the patterned CBL possesses highly uniform periodic microscale architectures, well-defined pixel boundaries, excellent dimensional repeatability, and steep sidewall profiles. These superior structural features effectively restrict the lateral spreading of functional layers, guaranteeing reliable pixel electrical isolation and high-fidelity pattern replication. Optical and fluorescence microscopy characterizations (Figures 6j-o, Figure S11 and Figure S12) further confirm the successful fabrication of highly uniform QD patterns with sharp edge contours, homogeneous luminous intensity, as well as negligible fluorescence quenching, pixel crosstalk, and interfacial edge diffusion. The optimized patterning strategy enables a minimum feature size of 1.5 μm, satisfying the dimensional requirement for high-resolution micro-display pixels.

As presented in Figure 7a, the fabricated patterned devices realize high-fidelity display visualization with sharp, defect-free edges and scalable ultra-high-resolution QD pixel arrays. Graded ultra-high pixel densities of 2,540, 5,644 and 10,160 PPI are

successfully achieved, and all patterned arrays exhibit excellent pixel uniformity and stable electroluminescence output. Normalized EL spectra (Figure 7b) display nearly identical emission peak positions and spectral profiles under varied driving voltages, demonstrating superior spectral stability of the patterned tandem QLEDs. Meanwhile, the BPAF-modified patterned device delivers higher current density and luminance than the pristine counterpart across the full operating voltage range (Figure 7c), further confirming that BPAF interfacial engineering substantially promotes charge generation efficiency and optimizes interfacial carrier transport kinetics. Notably, the optimized tandem device delivers an ultralow turn-on voltage of 2.0 V, a value comparable to that of single-junction QLEDs. This outstanding characteristic greatly simplifies the circuit design of low-voltage pixel driving systems. Furthermore, the optimized patterned device achieves a comprehensive enhancement in optoelectronic efficiency, with the maximum EQE increased from 30.86% to 42.82% (Figure 7d) and the corresponding power efficiency improved from 42 lm W^{-1} to 59 lm W^{-1} (Figure 7e). Remarkably, this optimized EQE value ranks among the highest reported values for high-resolution patterned QLEDs to date. It is worth noting that, benefiting from the ultralow driving voltage of our high-resolution devices, their power efficiency far outperforms that of unpatterned counterparts as shown in Figure 5e. These striking results collectively verify that patterned tandem QLEDs with BPAF interfacial modification retain outstanding spectral purity and stable optoelectronic performance even at ultrahigh PPI, fundamentally overcoming the long-standing power consumption and efficiency-resolution trade-off that limits conventional high-resolution QLEDs.

Table 2. Performance comparison of high-resolution QLEDs between this work and previously reported studies[8,52–55].

EQE_{max} (%)	Pixel density (PPI)	Reference
14.7	9,072	Ref. 54
15.6	3,031	Ref. 52
17.0	16,9333	Ref. 8
26.1	12,700	Ref. 55
24.2	5,080	Ref. 53
42.82	**10,160**	**This Work**

Conclusion

In conclusion, this work develops a facile molecular interfacial modulation strategy by incorporating strong electron-withdrawing BPAF molecules into ZnO electron transport layers, realizing the synergistic optimization of interfacial energy-level alignment and chemical microenvironment of CGLs for solution-processed tandem QLEDs. Specifically, BPAF incorporation triggers comprehensive downward shift of ZnO energy bands, which fundamentally optimizes the interfacial energy matching of CGL heterojunctions, substantially lowers the interfacial charge generation barrier, and facilitates efficient in-situ carrier generation and spatial separation. Meanwhile, the fluorine-rich functional groups of BPAF enable robust passivation of intrinsic oxygen vacancy defects in ZnO, significantly suppressing interfacial trap-assisted non-radiative recombination losses within CGLs. Benefiting from these synergistic electronic structure regulation and defect passivation effects, the fabricated ultra-high-resolution patterned QLEDs with a pixel density of 10,160 PPI deliver a record-high peak EQE of

42.82% with a low turn-on voltage of 2.0 V. This work fundamentally resolves the dual bottlenecks of severe energy-level mismatch and defect-dominated non-radiative recombination within CGLs, breaking the inherent efficiency-resolution trade-off that has long restricted the performance of conventional high-resolution QLEDs. The proposed universal molecular modulation strategy provides a facile, reliable, and scalable pathway for the rational design and fabrication of high-efficiency, ultra-high-resolution tandem QLEDs, paving the way for the industrial deployment of next-generation AR/VR-oriented micro-display systems.

Experimental Section

Materials

ITO-coated glass substrates were purchased from South China Technology Co., Ltd. PEDOT:PSS, TFB, and ZnO nanoparticles were provided by Xi'an Yuri Solar Energy Co., Ltd. Commercial red-emitting CdSe/ZnS core–shell QDs were obtained from Guangdong Pujiafu Optoelectronic Technology Co., Ltd. BPAF, n-octane, toluene, and ethanol were all sourced from Aladdin Reagent. All chemical reagents were utilized as received without additional purification or further modification.

Device Fabrication

Initially, a charge barrier layer (CBL) was fabricated via standard photolithography to effectively suppress device leakage current. The PEDOT:PSS serving as the hole injection layer (HIL) was spin-coated at 4000 rpm and annealed at 130 °C, followed by the deposition of the TFB HTL at 4000 rpm with identical thermal treatment.

Afterwards, the QD emissive layer was spin-coated at 2000 rpm and thermally treated at 80 °C, while ZnO:BPAF was spin-coated at 3000 rpm as the electron transport layer (ETL) and annealed at 80 °C. The BPAF is dissolved in ethanol to prepare a solution with a concentration of 3 mg/mL, which is then added into ZnO at a volume ratio of 1:10 between the solution and ZnO. For the fabrication of tandem architectures, upper functional multilayers were sequentially deposited through repeated solution spin-coating and low-temperature annealing processes. Specifically, the PEDOT:PSS interlayer was spin-coated at 4000 rpm and annealed at 80 °C, and the TFB layer was subsequently spin-coated at 4000 rpm and annealed at 80 °C. Thereafter, the second QD emissive layer was spin-coated at 2000 rpm and thermally cured at 80 °C, followed by the deposition of the ZnO ETL at 3000 rpm and annealing at 80 °C. Finally, silver (Ag) top electrodes were deposited by high-vacuum thermal evaporation to complete the fabrication of tandem QLED devices.

Characterization

The surface morphology and microstructure of ZnO films and patterned pixel arrays were characterized via scanning electron microscopy (Verios G4) and atomic force microscopy (Bruker Dimension Edge, Multimode 8). C-V and I-V measurements were conducted using a semiconductor characterization system (4200-SCS). Fourier transform infrared spectra were acquired on a Thermo Nicolet Avatar iS50 spectrometer to analyze molecular functional group interactions. Fluorescence microscopic morphologies of patterned QD films were recorded with an Olympus BX51M

fluorescence microscope. Photoluminescence spectra were measured using a fluorescence spectrophotometer (Hitachi F-4600), while photoluminescence quantum yields (PLQY) were determined using an XPQY-eq E-350-1100 commercial testing system. Time-resolved photoluminescence (TRPL) decay kinetics were characterized via an FLS1000 steady-state and time-resolved fluorescence spectrometer. The optical absorption properties of QD solutions and functional films were evaluated using a UV-Vis spectrophotometer (UV-3600, Cary 7000). Furthermore, the EL spectra of QLED devices were collected by an Ocean Optics USB2000+ fiber optic spectrometer. The device luminance, current density-voltage-luminance (J-V-L) curves, and external quantum efficiency (EQE) were comprehensively measured through a testing system consisting of a Keithley 2400 source meter, a fiber optic integrating sphere, and a matching spectrometer.

Conflicts of interest

The authors declare no conflict of interest.

Acknowledgments

This work was supported by the National Key Research and Development Program of China (2022YFB3606502).

Reference

1. Dai, X., Deng, Y., Peng, X. & Jin, Y. Quantum-Dot Light-Emitting Diodes for Large-Area Displays: Towards the Dawn of Commercialization. *Adv. Mater.* **29**, 1607022 (2017).
2. Jha, R. K., Kim, H. & Cho, S.-Y. Light outcoupling strategies for quantum dot light-emitting diodes. *Nanoscale* **18**, 2916–2941 (2026).
3. Kim, T.-H. *et al.* Full-colour quantum dot displays fabricated by transfer printing. *Nat. Photonics* **5**, 176–182 (2011).
4. Shirasaki, Y., Supran, G. J., Bawendi, M. G. & Bulović, V. Emergence of colloidal quantum-dot light-emitting technologies. *Nat. Photonics* **7**, 13–23 (2013).
5. Utzat, H. *et al.* Coherent single-photon emission from colloidal lead halide perovskite quantum dots. *Science* **363**, 1068–1072 (2019).
6. Wang, H. *et al.* High-efficiency and high-resolution patterned quantum dot light emitting diodes by electrohydrodynamic printing. *Nanoscale Adv.* **5**, 1183–1189 (2023).
7. Yang, K. *et al.* High-resolution and high-performance full-color electroluminescent quantum dot light-emitting diodes. *Nano Energy* **138**, 110817 (2025).
8. Cao, W. *et al.* Ultrahigh-resolution nanoimprint patterning of quantum-dot light-emitting diodes via capillary self-assembly. *Nat. Photonics* **20**, 301–309 (2026).
9. Sun, Q. *et al.* Bright, multicoloured light-emitting diodes based on quantum dots. *Nat. Photonics* **1**, 717–722 (2007).
10. Mashford, B. S. *et al.* High-efficiency quantum-dot light-emitting devices with enhanced charge injection. *Nat. Photonics* **7**, 407–412 (2013).

11. Coe-Sullivan, S., Liu, W., Allen, P. & Steckel, J. S. Quantum Dots for LED Downconversion in Display Applications. *ECS J. Solid State Sci. Technol.* **2**, R3026–R3030 (2013).

12. Lin, L. *et al.* Tailoring confinement and edge effects for enhancing performance in ultrahigh resolution quantum dot LEDs. *Chem. Eng. J.* **530**, 173440 (2026).

13. Chen, S. *et al.* On the degradation mechanisms of quantum-dot light-emitting diodes. *Nat. Commun.* **10**, 765 (2019).

14. David, A., Young, N. G., Hurni, C. A. & Craven, M. D. Quantum Efficiency of III-Nitride Emitters: Evidence for Defect-Assisted Nonradiative Recombination and its Effect on the Green Gap. *Phys. Rev. Appl.* **11**, 031001 (2019).

15. Lee, H. Degradation Mechanisms in Quantum-Dot Light-Emitting Diodes: A Perspective on Nondestructive Analysis. *Int. J. Mol. Sci.* **26**, 10465 (2025).

16. Bao, H. *et al.* Quantitative Determination of Charge Accumulation and Recombination in Operational Quantum Dots Light Emitting Diodes via Time-Resolved Electroluminescence Spectroscopy. *J. Phys. Chem. Lett.* **14**, 1777–1783 (2023).

17. Chen, J., Ma, D., Liu, Y. & Wang, Y. Studies of kinetics of charge carrier recombination in organic light-emitting diodes based on beryllium complexes by transient electroluminescence. *J. Phys. Appl. Phys.* **38**, 3366–3370 (2005).

18. Amin, A., Hong, J., Jang, J., Hwang, I. & Lee, J. Unified Analysis of Transient Electroluminescence in Organic Light-Emitting Diodes: Deciphering Charge Transport and Emission Dynamics. *Adv. Opt. Mater.* **13**, e02153 (2025).

19. Zhong, C. *et al.* Ultrahigh-Resolution Full-Color Quantum Dot LEDs Based on Region-Selective Interfacial Self-Assembly. *Adv. Funct. Mater.* **35**, 2510076 (2025).
20. Dai, X. *et al.* Solution-processed, high-performance light-emitting diodes based on quantum dots. *Nature* **515**, 96–99 (2014).
21. Gao, H. *et al.* High-performance, high-resolution quantum dot light-emitting devices through photolithographic patterning. *Org. Electron.* **108**, 106609 (2022).
22. Zheng, W. *et al.* Performance improvements in all-solution processed inverted QLEDs realized by inserting an electron blocking layer. *Nanotechnology* **32**, 335204 (2021).
23. Zhang, X. *et al.* Boosting the Efficiency of High-Resolution Quantum Dot Light-Emitting Devices Based on Localized Surface Plasmon Resonance. *ACS Appl. Mater. Interfaces* **16**, 13219–13224 (2024).
24. Yan, X. *et al.* Quantifying Efficiency Roll-Off Factors in Quantum-Dot Light-Emitting Diodes. *Adv. Sci.* **11**, 2410041 (2024).
25. Li, D. *et al.* Exciton management and balanced charge-carrier transport enable efficient organic field-effect light-emitting transistors. *Nat. Photonics* **20**, 109–118 (2026).
26. Fung, M., Li, Y. & Liao, L. Tandem Organic Light-Emitting Diodes. *Adv. Mater.* **28**, 10381–10408 (2016).
27. Meng, S. *et al.* Dipole Engineering in Charge Generation Interface for Fully Solution-Processed and PEDOT:PSS-Free Tandem Quantum-Dot Light-Emitting Diodes. *Adv. Electron. Mater.* **11**, 2500180 (2025).

28. Yu, K. *et al.* Embankment Protection-Inspired Interfacial Engineering for Ultrahigh-Efficiency, Stable Tandem Quantum Dot Light-Emitting Devices.
29. Zhou, T. *et al.* High-Performance Tandem Quantum-Dot Light-Emitting Diodes Based on Bulk-Heterojunction-Like Charge-Generation Layers. *Adv. Mater.* **36**, 2313888 (2024).
30. Jing, Y. *et al.* Photolithographic fabrication of high-resolution Micro-QLEDs towards color-conversion microdisplay. *Light Sci. Appl.* **14**, 370 (2025).
31. Park, B. *et al.* Multi-Functional Electrophoretic Deposition for Crosstalk-Free, Ultra-High-Resolution Full-Color QLEDs. *Laser Photonics Rev.* **20**, e02567 (2026).
32. Zhou, D. *et al.* Coverage- and Temperature-Dependent Adsorption of Phenol on the ZnO(10 1^{-} 0) Surface. *J. Phys. Chem. C* **128**, 1685–1693 (2024).
33. Jia, S. *et al.* Optimizing ZnO–Quantum Dot Interface with Thiol as Ligand Modification for High-Performance Quantum Dot Light-Emitting Diodes (Small 13/2024). *Small* **20**, 2470106 (2024).
34. Gupta, D. *et al.* Defects engineering and enhancement in optical and structural properties of 2D-MoS2 thin films by high energy ion beam irradiation. *Mater. Chem. Phys.* **276**, 125422 (2022).
35. Ranjuna, M. K. & Balakrishnan, J. High temperature anomalous Raman and photoluminescence response of molybdenum disulfide with sulfur vacancies. *Sci. Rep.* **13**, 16418 (2023).
36. Miller, B. *et al.* Tuning the Fröhlich exciton-phonon scattering in monolayer MoS2. *Nat. Commun.* **10**, 807 (2019).

37. Höfle, S. *et al.* Charge Generation Layers for Solution Processed Tandem Organic Light Emitting Diodes with Regular Device Architecture. *ACS Appl. Mater. Interfaces* **7**, 8132–8137 (2015).

38. Guo, Q. *et al.* Charge generation mechanism of tandem organic light emitting diodes with pentacene/C_{70} organic heterojunction as the connecting layer. *J. Mater. Chem. C* **4**, 376–382 (2016).

39. Kim, B. S., Chae, H., Chung, H. K. & Cho, S. M. Electrical and optical analyses of tandem organic light-emitting diodes with organic charge-generation layer. *AIP Adv.* **8**, 065303 (2018).

40. Qu, X. & Sun, X. Impedance spectroscopy for quantum dot light-emitting diodes. *J. Semicond.* **44**, 091603 (2023).

41. Chulkin, P. In-Situ Characterisation of Charge Transport in Organic Light-Emitting Diode by Impedance Spectroscopy. *Electron. Mater.* **2**, 253–273 (2021).

42. Magar, H. S., Hassan, R. Y. A. & Mulchandani, A. Electrochemical Impedance Spectroscopy (EIS): Principles, Construction, and Biosensing Applications. *Sensors* **21**, 6578 (2021).

43. Laschuk, N. O., Easton, E. B. & Zenkina, O. V. Reducing the resistance for the use of electrochemical impedance spectroscopy analysis in materials chemistry. *RSC Adv.* **11**, 27925–27936 (2021).

44. Lin, Y.-J. Comment on “Schottky contact on a ZnO (0001) single crystal with conducting polymer” [Appl. Phys. Lett. 91, 142113 (2007)]. *Appl. Phys. Lett.* **92**, 046101 (2008).

45. Karak, S., Lim, J. A., Ferdous, S., Duzhko, V. V. & Briseno, A. L. Photovoltaic Effect at the Schottky Interface with Organic Single Crystal Rubrene. *Adv. Funct. Mater.* **24**, 1039–1046 (2014).

46. Chung, D. S. *et al.* Significant Lifetime Enhancement in QLEDs by Reducing Interfacial Charge Accumulation via Fluorine Incorporation in the ZnO Electron Transport Layer. *Nano-Micro Lett.* **14**, 212 (2022).

47. Lin, Y.-H. *et al.* Deciphering photocarrier dynamics for tuneable high-performance perovskite-organic semiconductor heterojunction phototransistors. *Nat. Commun.* **10**, 4475 (2019).

48. Zhang, J., Zhu, X., Wang, M. & Hu, B. Establishing charge-transfer excitons in 2D perovskite heterostructures. *Nat. Commun.* **11**, 2618 (2020).

49. Yang, D. *et al.* Regular Tandem Quantum Dot Light-Emitting Diodes with over 51% External Quantum Efficiency for Next-Generation Displays. *Adv. Mater.* **37**, e08173 (2025).

50. Sun, Y. *et al.* Fully solution-processed red tandem quantum dot light-emitting diodes with an EQE exceeding 35%. *J. Mater. Chem. C* **12**, 10053–10060 (2024).

51. Meng, S. *et al.* Solution-Processed Tandem Quantum-Dot Light-Emitting Diodes with Dual Charge Generation Interfaces: Achieving Over Threefold Efficiency Enhancement. *Adv. Mater. Interfaces* **11**, 2400098 (2024).

52. Luo, C. *et al.* High-Resolution, Highly Transparent, and Efficient Quantum Dot Light-Emitting Diodes. *Adv. Mater.* **35**, 2303329 (2023).

53. Zhang, C. *et al.* Pixelated quantum-dot superlattice LEDs. *Nature* **652**, 1173–1180

(2026).

54. Meng, T. *et al.* Ultrahigh-resolution quantum-dot light-emitting diodes. *Nat. Photonics* **16**, 297–303 (2022).

55. Lin, L. *et al.* Nanoscale transfer-printed full-colour ultrahigh-resolution quantum dot LEDs. *Nature* **652**, 349–358 (2026).

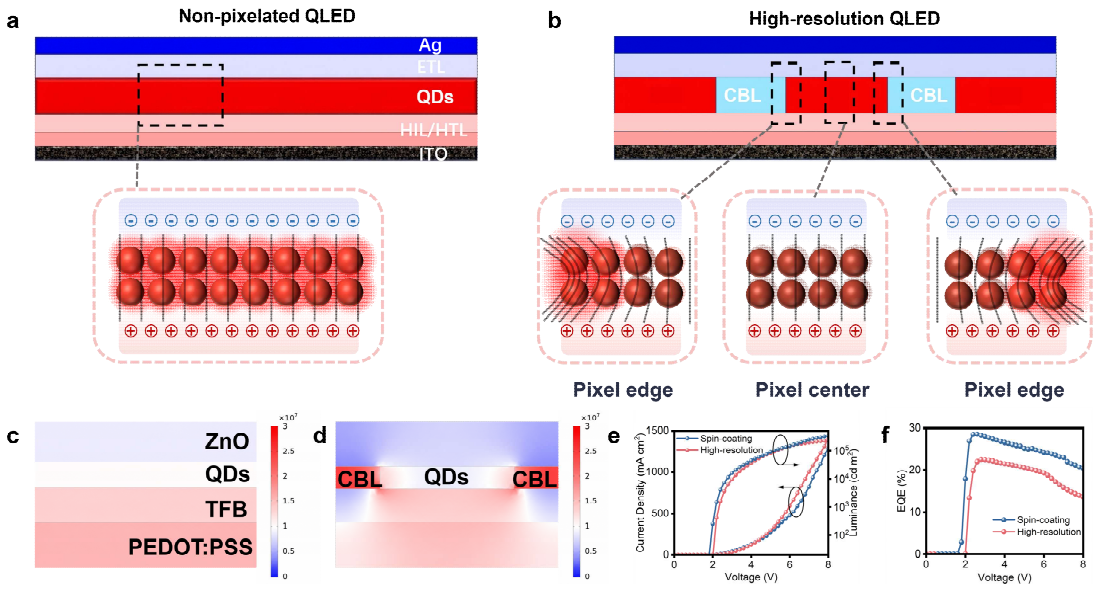


Figure 1. Structural, electric field distribution and optoelectronic performance comparison between non-pixelated QLED and high-resolution QLED. (a) Schematic cross-section of conventional full-area spin-coated QLED, together with the uniform internal electric field distribution within QD emission layer. (b) Device architecture of high-resolution pixelated QLED integrated with lateral CBLs at pixel boundaries, illustrating severe fringe electric field distortion at pixel edges and homogeneous electric field at pixel center. (c, d) Two-dimensional mappings of electric field intensity across the vertical cross-section for non-pixelated QLED and high-resolution QLED, respectively. (e, f) J-V-L and EQE-V curves of the two devices.

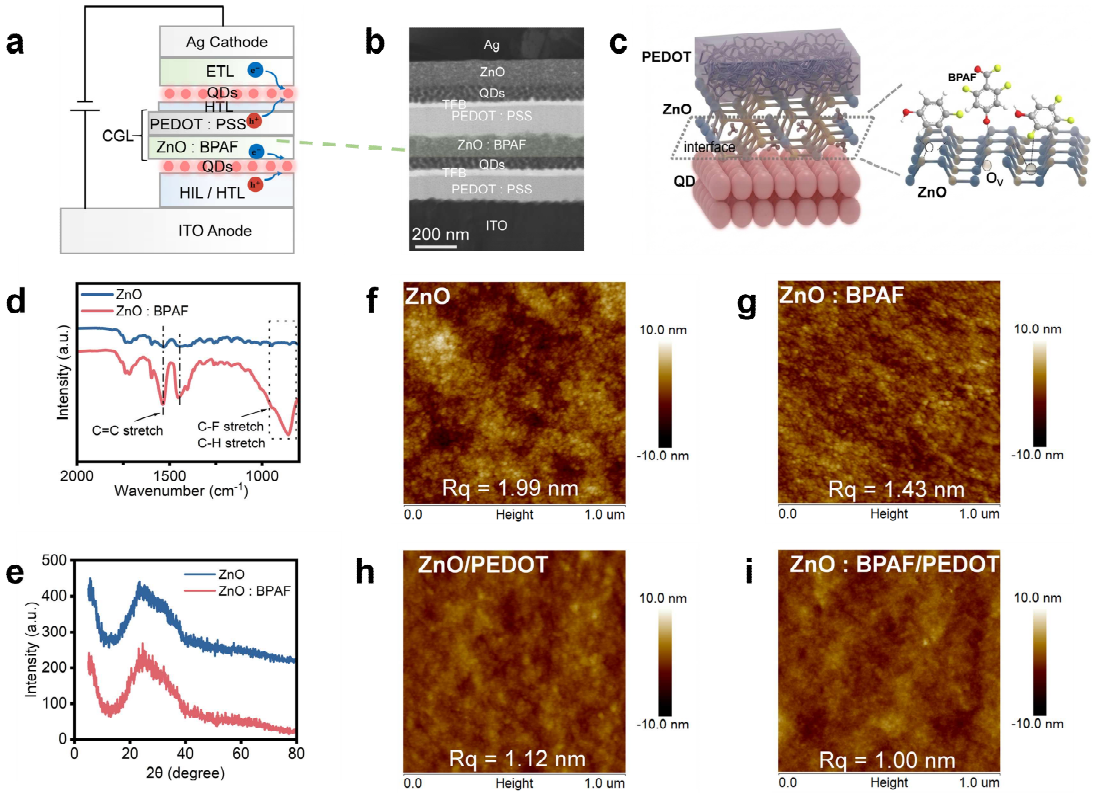


Figure 2. (a) Schematic illustration of the tandem QLED configuration and corresponding carrier transport pathways. (b) Cross-sectional TEM image of the multilayer stacked tandem QLED structure. (c) Schematic of defect modification by BPAF at the ZnO/QD interface. (d, e) FTIR spectra and XRD patterns of pristine ZnO and ZnO:BPAF films. (f-i) AFM images of the corresponding films.

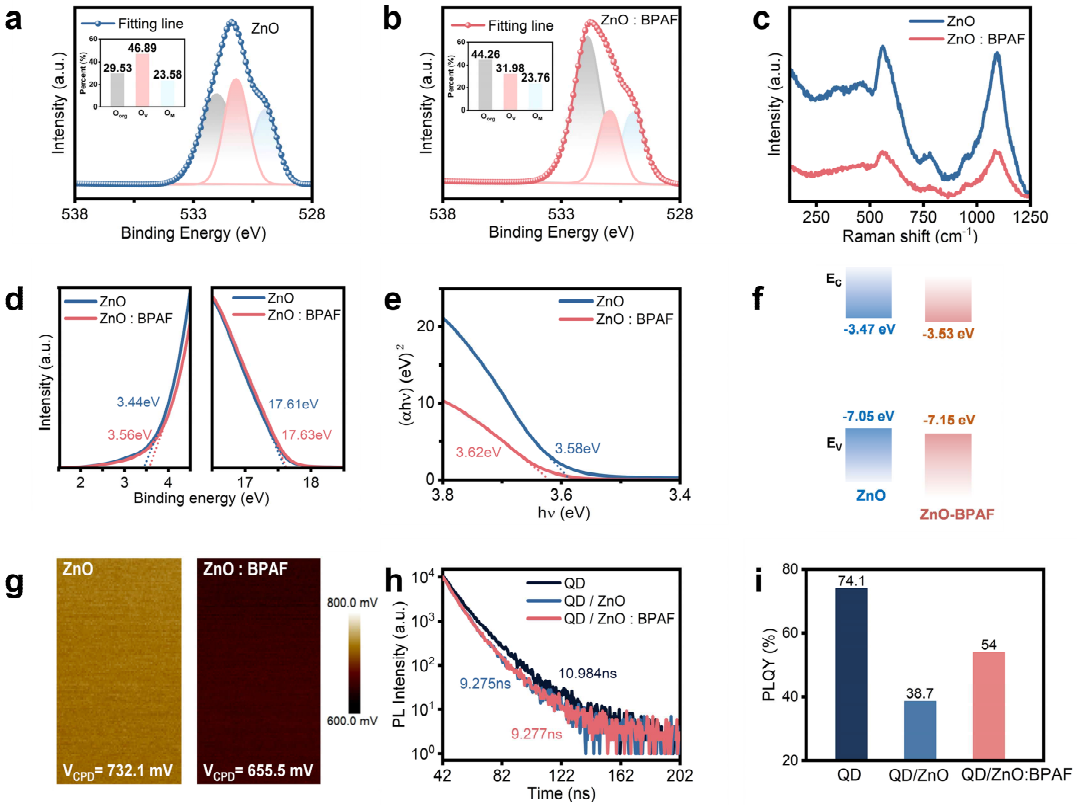


Figure 3. (a, b) High-resolution O 1s XPS spectra of ZnO and ZnO:BPAF films. (a, b) High-resolution O 1s XPS spectra of pristine ZnO and ZnO:BPAF films. (d, e) UPS spectra and corresponding optical band gaps calculated from UV-Vis absorption results. (f) Energy-level alignment diagram based on UPS and UV-Vis measurements. (g) KPFM surface potential distribution maps of ZnO and ZnO:BPAF films. (h, i) TRPL decay curves and corresponding PLQYs of QD layers deposited on blank quartz, pristine ZnO, and ZnO:BPAF substrates.

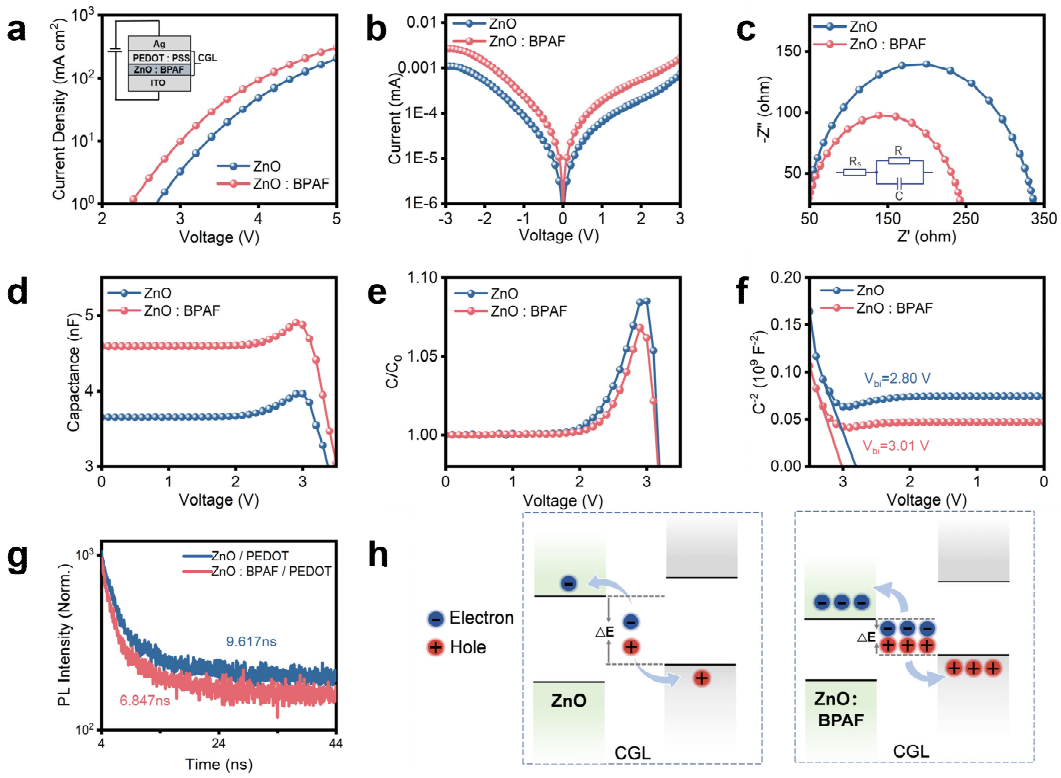


Figure 4. Electrical and kinetic characterizations of pristine and BPAF-modified CGLs. (a) J-V characteristics of standalone CGL devices (inset: structural schematic of the CGL-only device). (b) Bipolar I-V characteristics of the CGL devices. (c) Nyquist plots obtained from EIS measurements. (d, e) C-V curves of CGL devices (C_0 represents the geometric capacitance). (f) Mott-Schottky plots of different CGL films. (g) TRPL decay dynamics of pristine and modified CGL heterointerfaces. (h) Schematic illustration of the charge generation, interfacial separation, and directional transport mechanism within CGLs.

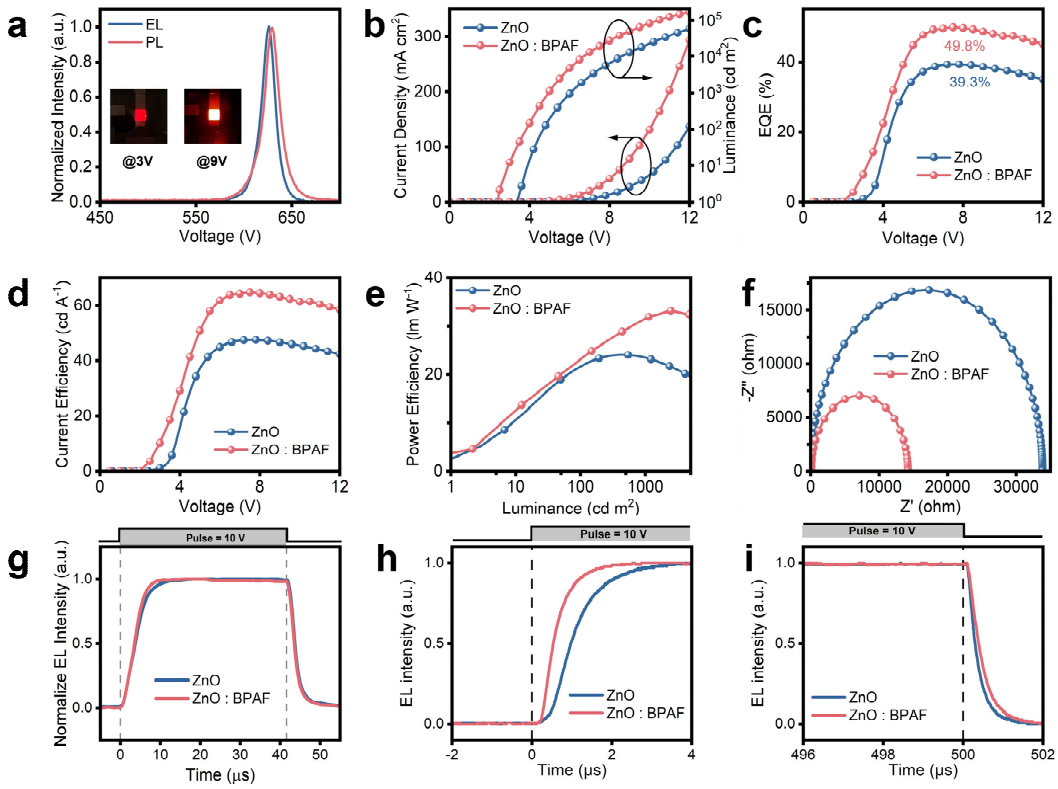


Figure 5. Comprehensive optoelectronic performance and dynamic carrier transport behaviors of pristine and BPAF-modified tandem QLEDs. (a) Normalized EL and PL spectra (inset: corresponding EL emission photographs). (b-e) J-V-L characteristics, (c) EQE-L, (d) CE-L and (e) PE-L curves. (f) Frequency-dependent Nyquist plots of different devices. (g-i) Transient EL response behaviors: (g) full-cycle transient EL profiles; (h) magnified rising-edge dynamic responses; (i) magnified falling-edge dynamic responses.

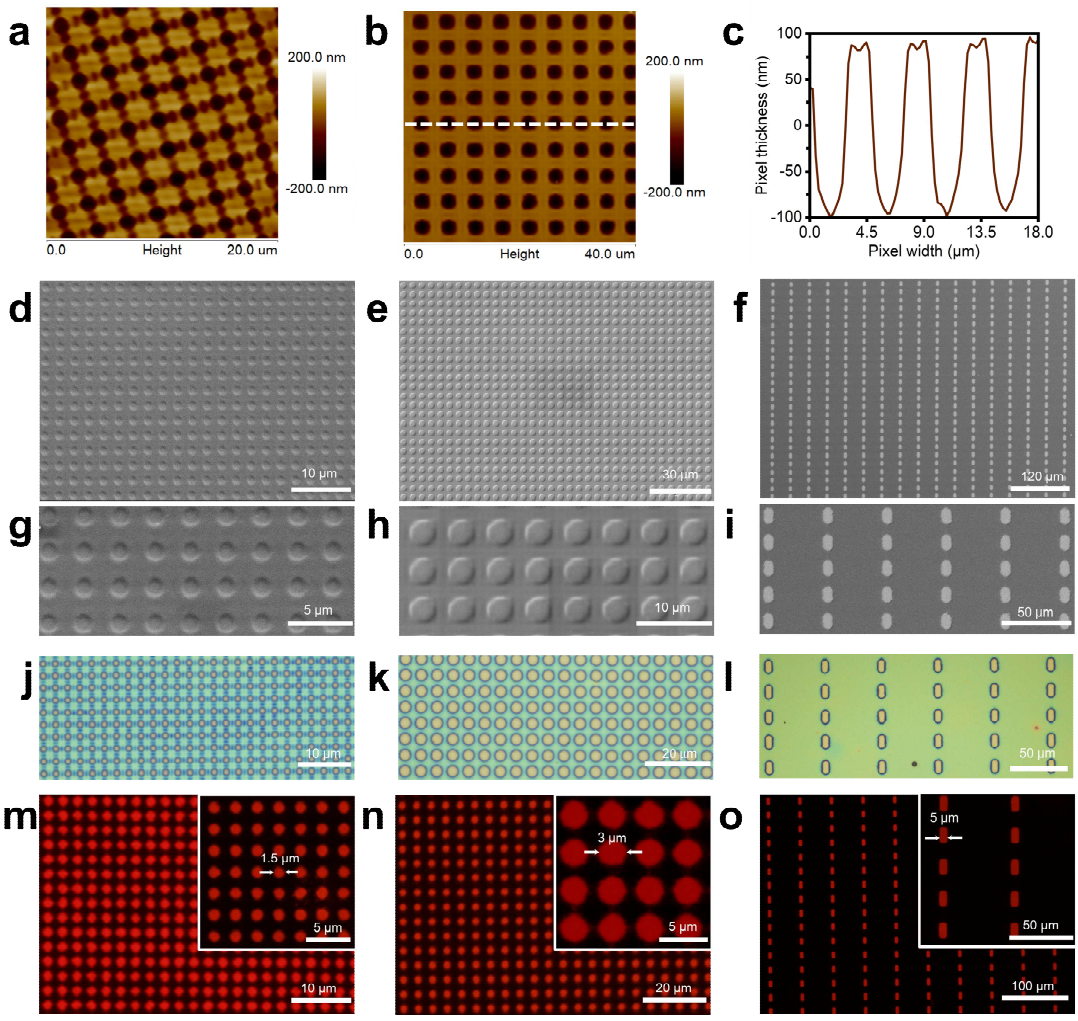


Figure 6. Morphological and patterning characterization of patterned CBL and QD pixel arrays. (a, b) AFM height images of the patterned CBL structure. (c) Corresponding height profile extracted along the dashed line in (b). (d-i) SEM images of QD pixel arrays with varied sizes and geometric configurations. (j-l) Optical microscope images of patterned QD pixels. (m-o) Fluorescence microscope images of patterned QD emissive films.

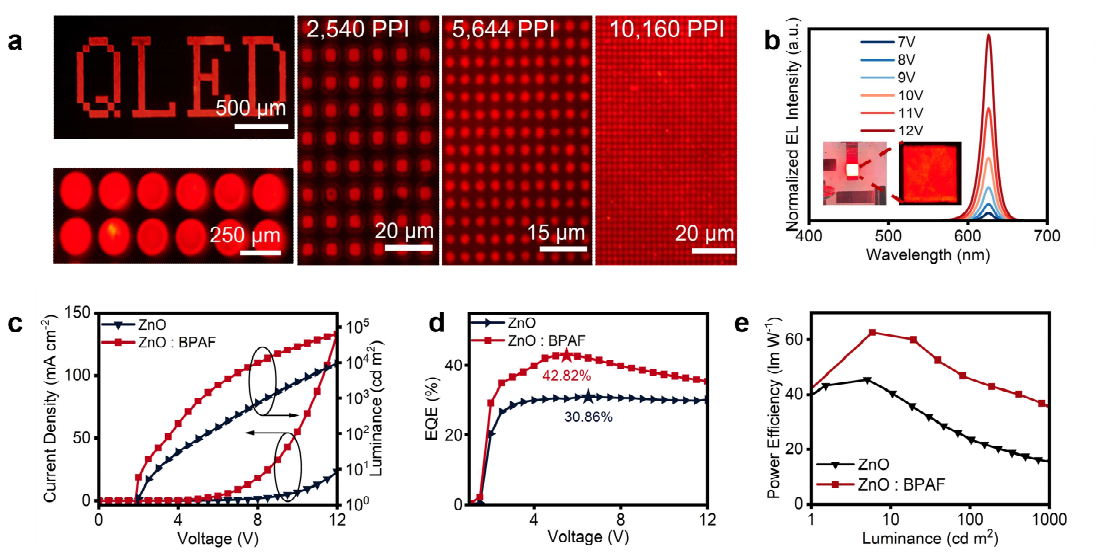


Figure 7. Optoelectronic performance of high-resolution patterned tandem QLEDs. (a) EL emission images of patterned QLED arrays with different pixel densities. (b) Normalized EL spectra measured under varied driving voltages. (c) J-V-L, (d) EQE-V, and (e) CE-L curves of patterned QLEDs with a minimum pixel size of 1.5 μm.

Supplementary Files

This is a list of supplementary files associated with this preprint. Click to download.

- SupportingInformation.docx